Journal of Materials Processing Tech. 298 (2021) 117318

Contents lists available at ScienceDirect

Journal of Materials Processing Tech.

journal homepage: www.elsevier.com/locate/jmatprotec

Failure mechanism analysis based on laser-based surface treatments for aluminum-polyamide laser joining

Mahdi Amne Elahi [a,*], Marcus Koch [b], Julien Bardon [c], Frédéric Addiego [c], Peter Plapper [a]

[a] University of Luxembourg, FSTM - Faculty of Science, Technology and Medicine, Luxembourg
[b] INM - Leibniz Institute for New Materials, Campus D2 2, 66123 Saarbrücken, Germany
[c] LIST - Luxembourg Institute of Science and Technology, Materials Research and Technology Department, Luxembourg

ARTICLE INFO

Associate Editor: Hui-Ping Wang

Keywords:
Laser joining of aluminum-polyamide
Surface pre-treatment
Laser polishing
Failure mechanism

ABSTRACT

The development of strong metal to polymer assemblies is currently an important research subject thanks to its prominence to develop lightweight structures. Furthermore, laser welding is known to be a fast, reliable, and versatile joining process, and it was demonstrated recently that it can be applied to such metal to polymer systems. To enhance the mechanical properties of the laser-joined aluminum-polyamide (Al-PA) specimens, laser polishing and laser ablation processes have been implemented on the aluminum surface before joining. The polyamide surface was also treated with the laser beam, separately. The surfaces were tested by several characterization techniques before and after each surface treatment. Then aluminum and polyamide samples with different surface treatments have been joined with an identical laser joining process. The mechanical properties of the joints in single lap shear configuration are reported and the failure mechanisms are discussed based on micro-computed x-ray tomography imaging of joined specimens and microscopic analysis before failure. Results show that both surface treatments of aluminum significantly improve the shear load of the joint; however, with different failure mechanisms. Polyamide surface treatment and increasing degree of crystallinity are effective when combined with the laser polishing of the Al surface. This combination is responsible for further enhancement of the shear load of the joint to the limit of base metal strength which is approximately 60 % improvement compared to the untreated samples. Finally, energy dispersive X-ray mapping shows the physicochemical bonding between aluminum oxide and polyamide at the interface.

1. Introduction

The application of lightweight hybrid metal-polymer components has gained considerable attention to achieve functionalization and weight reduction for structural applications. Therefore, joining technology is a fundamental factor to achieve this aim. Hybrid metal-polymer assemblies can be obtained by several processes like mechanical fastening, adhesive bonding, or welding. Among them, welding seems more promising for some industrial applications thanks to its unique advantages like the elimination of adhesives or joining elements; the former being possibly toxic and the latter bringing additional weight to the assembly. The exceptional control over the heat input made the laser joining suitable to join metals to polymers. The laser-assisted metal-polymer (LAMP) joining is introduced by Katayama and Kawahito (2008). Still, it is well known that to achieve a robust joint, surface treatment is necessary, either on the metal or on the polymer side. Heckert and Zaeh (2014) worked on laser-based metal pre-treatments in different scales of macroscopic, microscopic, and nanoscopic structures to increase the mechanical properties of the joints. Roesner et al. (2013) reported on the creation of undercut grooves on the metal to improve the mechanical properties of the joints thanks to the promotion of mechanical interlocking. Rodríguez-Vidal et al. (2016) also studied the effect of mechanical interlocking by surface treatment of the metal with a nanosecond pulsed laser and reported on the greatest strength of the joints when the distance between subsequent grooves was minimized. However, Heckert et al. (2015) reported on the significant effect of the oxide layer created by the pre-treatment process on cohesion improvement between aluminum and thermoplastic material. For polymer treatment, Arai et al. (2014) studied the effect of polymer surface chemical modification to improve the mechanical properties of the joints. Therefore, on the one hand, it is difficult to identify the contribution of metal and polymer treatments for a given material

* Corresponding author.
E-mail address: mahdi.amneelahi@uni.lu (M. Amne Elahi).

https://doi.org/10.1016/j.jmatprotec.2021.117318
Received 16 February 2021; Received in revised form 22 July 2021; Accepted 1 August 2021
Available online 2 August 2021

combination. On the other hand, the effect of mechanical interlocking and/or physicochemical bonding to achieve a reliable joint is challenging.

Considering polyamide is a heat-sensitive material; some studies discussed the presence of gas bubbles near the interface of metal/polymer due to polymer thermal pyrolysis. Tan et al. (2015) studied the formation mechanisms of different types of porosities near the interface of metal/polymer during the laser joining process. Yusof et al. (2012) investigated the temperature measurement during the process and reported the thermal decomposition of the polymer at high heat input that results in bubble formation. On the one hand, Jung et al. (2013) suggested that the formation of the small bubbles can be positive since it expands the molten polymer and fills the metal surface structure. On the other hand, Lambiase and Genna (2017) reported on the negative effect of bubbles on the mechanical properties of the joints. In this regard, Chen et al. (2016) introduced an ultrasonic-aided LAMP process to avoid bubble formation and Wang et al. (2019) implemented a modified laser joining process to eliminate them. In the present study, some insights about the effect of bubble formation on assembly strength are also provided.

Schricker et al. (2021) also studied the joining zone of metal/-polymer and discussed the effect of polymer heat treatment during the laser joining process. Secondary crystallization was observed, and it is responsible for the modification of polymer morphology and mechanical properties.

The effect of the surface roughness is contradictory among several reports: Bauernhuber and Markovits (2012) reported on the positive effect of the metal surface roughness on the mechanical properties of the joint while Bergmann and Stambke (2012) found no correlation between surface roughness and the shear strength. Therefore, it is interesting to perform a study on different surface treatments on aluminum, which leads to different roughness.

In previous studies, Amne Elahi et al. studied the joining with different modulated powers to prevent PA thermal degradation (2020) and compared miscellaneous surface treatment processes (abrasive--based and laser-based) regarding the mechanical properties of the joints and the mechanisms of failure (2021). However, a detailed study on a combination of surface treatments for both materials is not presented. Therefore, it is interesting to apply the optimum joining process and investigate the surface treatment of aluminum and polyamide to achieve superior mechanical properties of the assemblies. In this regard, another objective of the present study is to investigate the failure of these assemblies, by playing on the metal roughness, and try to understand how the failure happens according to the thermally affected zone characteristics in the polymer. Finally, the contribution of polymer surface modification before the joining process on the mechanical properties of the joints is studied.

2. Materials and methods

2.1. Materials and processes

For this study, 1050-H24 Aluminum alloy (simply named Al from now on in the paper) and industrial-grade extruded polyamide 6,6 (by Dutec) (simply named PA) have been used. All samples were cleaned with ethanol (≥99.8 %) before further processing. As the humidity content of PA affects the joint quality and the mechanical properties, PA samples were conditioned based on ISO 1110 standard. Accordingly, before joining, the humidity content is lower than 0.1 %. Two different Al laser pre-treatment were considered before joining. The laser ablation process has been carried out on the as-received Al surface with a pulsed wave (PW) TruMark 6130 laser machine (laser medium: Nd:YVO_4, wavelength:1064 nm, and beam quality: M^2<1.2). The laser polishing process has been implemented on the as-received Al surface with a continuous wave (CW) fiber laser (TruFiber - max power of 400 W - with the wavelength of 1070 nm equipped with Scanlab HS20 2D f-θ scanner head to achieve a beam quality of $M^2 = 1.03$), while PA surface treatment was done with a CW CO_2 laser (laser station TM020+ with the wavelength of 10.6 μm and max power of 25 W equipped with SCANcube 10 scanner head). Fig. 1 shows the schematics also the appearance of the laser treatment processes.

The laser polishing process for Al aims to melt a very thin layer of the material on the surface and consequently reduce the surface asperities by surface tension. Considering Al is a highly reflective material to process with the laser beam, a near-infrared CW laser with a high beam quality was applied to achieve a homogeneous melted layer and reduce the surface roughness effectively with a single-step process. The corresponding parameters such as scanning speed were optimized by the design of experiments (DOE) to minimize the roughness amplitude (Ra) and avoid damaging the sample during the process. A similar process was designed for PA surface treatment with a low-power CO_2 laser as the reflectivity is not critical for PA and to melt a thin layer on the surface, low power is required. Regarding the laser ablation process, the idea is to apply the laser beam in short pulses with high peak power to evaporate the material and increase the surface roughness.

For the laser conduction joining process which was also carried out with the fiber laser, the Al and PA samples are placed in an overlap configuration and the laser beam is applied from the Al side, while the pre-treated areas are aligned to face each other. It is worth noticing that PA is not transparent to the laser beam, which prevents joining the assembly in laser transmission joining configuration. The laser joining process is identical for all samples: the laser joining parameters and the clamping pressure which is provided with four toggle clamps are kept constant and no shielding gas is applied for the joining nor the surface treatments processes. To better control the energy input to PA and widening the joining area, temporal and spatial modulations of laser beam have been implemented.

Fig. 2 shows the joining configuration and the temporal and spatial modulations. The treated area covers the whole surface of the corresponding material with a width of 10 mm to avoid the contribution of the as-received area during the laser joining process of the treated samples. For all laser-joined specimens, the modulation time and period are 26 and 40 μs, respectively. Consequently, the modulated power is 260 W. The laser joining parameters were selected based on a previous study (Amne Elahi et al., 2020) to ensure a robust joint without materials degradation due to excessive heat input (it is observed that above 300 W of modulated power with the current materials and configuration, the PA experiences degradation).

2.2. Characterization methods

Al and PA surfaces with different treatments were characterized by Environmental Scanning Electron Microscopy (ESEM) with FEI ESEM Quanta 400 FEG and Optical Microscopy (OM) was done with Leica DM 4000 M. PA surface crystallinity prior and after the treatment was investigated by grazing X-Ray Diffraction (gXRD) using a Panalytical X'Pert PRO MPD system. The incident angle was set to 0.5 ° engendering a penetration depth of 35 μm. The X-ray beam was generated at 40 kV and 45 mA through CuKα radiation (wavelength λ = 1.54 Å). The diffractograms were recorded in the 2θ range of 5 ° to 50 °, while the software Fityk was utilized to fit the experimental curves with the peak functions. To this end, the background signal was first subtracted, and then the amorphous scattering peak was positioned in the range of 21°–21.5 °. The amorphous peaks were modeled with a Voigt function. Six crystalline diffraction peaks ((102)α at 13.1 °, (200)α at around 20.4 °, $(001/20\bar{1}/200)\gamma$ at 22.4 °, $(002/\bar{2}00)\alpha$ at around 23.6 °, (202)α at around 38 °, and an unknown weak diffraction or scattering peak at 41.2 °) were modeled with Lorentzian functions (Penel Pierron, 1998). From the area of each peak, the overall weight index of crystallinity (ratio between the sum of all crystalline peak areas and the sum of all crystalline peak areas and the amorphous peak area), and the weight

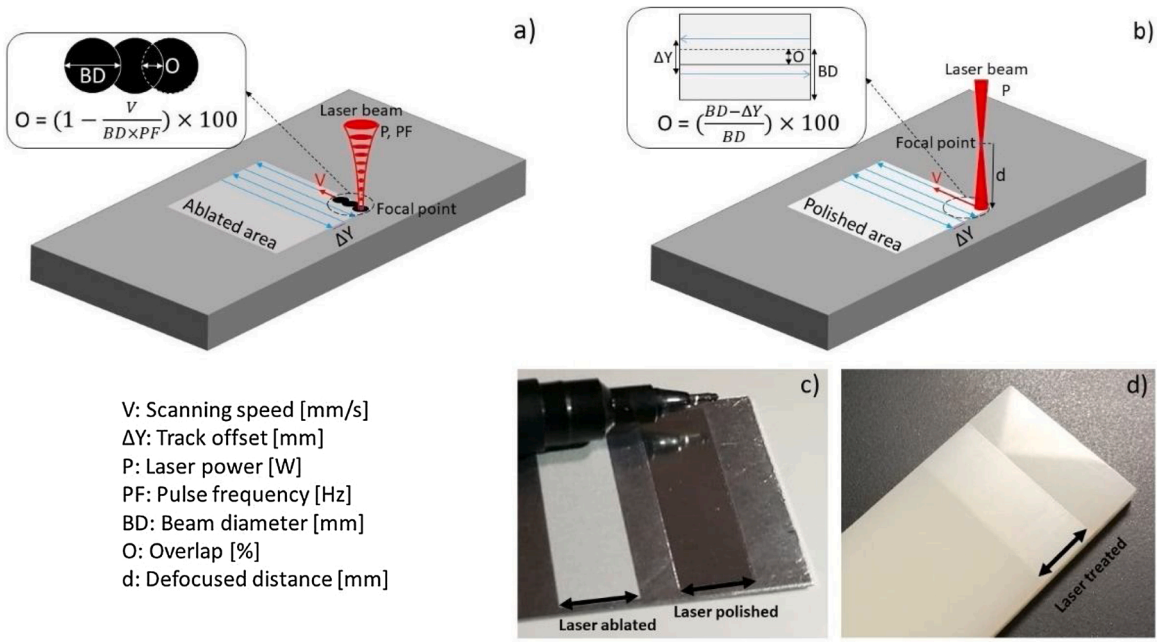

	Scanning speed [mm/s]	Track offset [mm]	Laser power [W]	Pulse frequency [kHz]	Beam diameter [mm]	Overlap [%]	Defocused distance [mm]
Laser ablation	1000	0.05	20 (P_O)	120	0.028	70	0
Al Laser polishing	2000	0.05	400 (CW)	-	0.08	37.5	3
PA Laser polishing	20000	0.01	25 (CW)	-	0.1	90	1

Fig. 1. Schematics of a) the laser ablation, b) the laser polishing (and the laser treatment of PA) processes (not to scale), with the corresponding parameters, c) the appearance of Al laser treatments, and d) PA laser treatment on as-received surfaces.

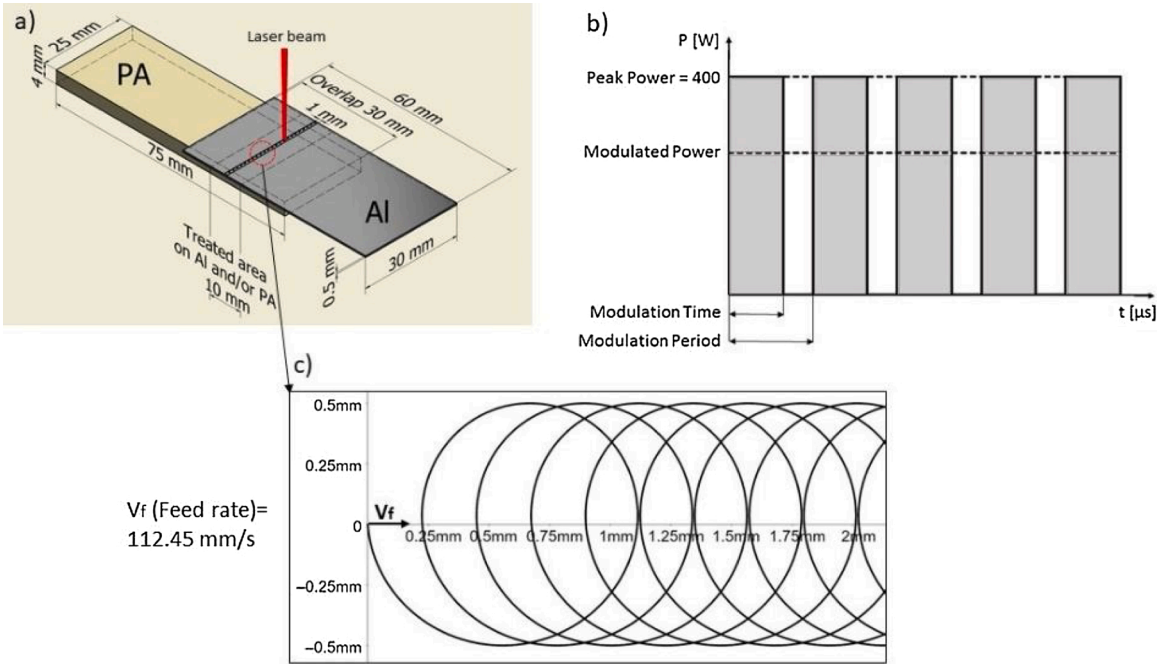

Fig. 2. a) Joining configuration, b) temporal modulation and c) spatial modulation of the laser beam.

fraction of each crystalline phase have been calculated.

PA surface chemistry was investigated by X-ray Photoelectron Spectroscopy (XPS) (with Kratos Axis Ultra DLD) before and after laser treatment. The same analysis was performed on Al before and after laser polishing. The take-off angle is 0 ° and the calibration is performed through the C1s peak whose value is taken at 285.0 eV. Two tests were performed per sample to assess reproducibility. For each test, the energy resolution was 1.5 eV for the survey spectrum, and it was 0.6 V for the high-resolution spectrum, which was performed on Al, C, O for aluminum samples, and N, C, O for PA samples.

The topography and nanomechanical properties were measured by Atomic Force Microscopy (AFM) with an MFP 3D infinity microscope from Asylum (Oxford instruments). Bimodal tapping measurements were carried out in an amplitude modulation frequency modulation (AMFM) mode (Kocun et al., 2017). Probes were AC 160 R3 from Asylum Research, whose resonance frequency and force constant were approximately 300 kHz and 26 N/m, respectively. Three sizes of images were performed with a 128 × 128-pixel resolution: "low magnification" images with the size of either 40 × 40 μ m^2 or 15 × 15 μ m^2 and "high magnification" images with the size of 1 × 1 μ m^2. Two samples were tested. The first sample is a PA that has been partly laser-treated, i.e., one part was laser-treated, and the other part was untreated. Since the surface nanostructure, probably assigned to crystallites, was not properly elucidated on the untreated area, a second sample was prepared by removing the first hundreds of nm of the surface (in thickness) by cryo-ultramicrotomy using a diamond knife. Imaging was done on the remaining flat block face of the material whose extremely low roughness enables to visualize the intrinsic nanostructure. Thereby, the interface between the untreated and treated parts is better defined, and the topography amplitude is much reduced, which allows better nanomechanical analysis and therefore better contrast between crystallites and amorphous volume. Microhardness tests were carried out by static indentation with a nano scratch tester (NST from Anton Paar). Indentation of 100 mN with a conosphere tip of 5 μm radius was performed. Residual imprints outside diameter were evaluated by optical microscopy and the corresponding hardness value was calculated as the ratio of the load divided by the imprint area.

Micro-computed X-ray Tomography (μCT) testing was performed to visualize the internal structure of the materials after the joining process. EasyTom 160 from RX Solutions has been utilized at 100 kV and 30 mA with a micro-focused tube (tungsten filament). The source-to-detector distance (SDD) and the source-to-object distance (SOD) were selected in such a way to obtain a voxel size of around 3 μm. The reconstruction of the sample volume has been conducted with the software Xact64 after applying geometrical corrections and ring artifact attenuation. The imaging of the reconstructed volume of the assembly has been done with the software Avizo. The analysis is focused on the interfacial region between Al and PA.

The tensile-shear test on the joints was performed in a single lap shear configuration using a Zwick/Roell machine with a maximum force of five kN. The test was done at a constant speed of 2.5 mm/min, free clamping length of 445 mm, and a fixture to limit the bending of the specimens. The fixture consists of carbon fiber-reinforced polymer (CFRP) material with a very smooth surface (Ra = 0.02 μm) to avoid friction with the sample (see Fig. 3). The Ra value of all the samples was measured using a Mitutoyo SJ-500 P with a Stylus tip radius of 2 μm based on ISO 4288-1996. The reported values of tensile-shear load (maximum force during the test) and the Ra measurement are representative of at least ten individual measurements.

TEM (Transmission Electron Microscopy) imaging of Al was done by a JEOL JEM-2100 LaB_6 after lamella preparation using a FEI Versa 3D. Sample preparation includes the coating of Al with Platinum (Pt) before using a Gallium ion beam for the lamella preparation. It should be noted that for laser-polished Al, an additional layer of amorphous carbon was deposited by evaporation before the Pt coating. Typically, the thickness of FIB lamella is in the range of 60 nm.

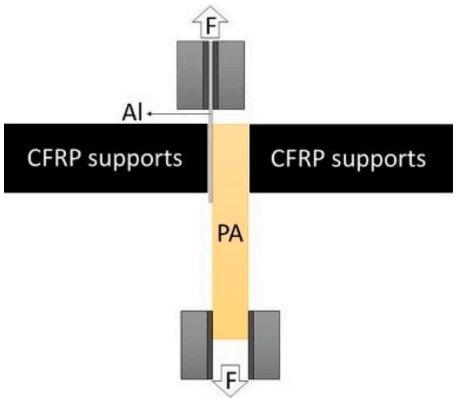

Fig. 3. The schematics of the tensile-shear test with the designed fixture to limit the bending of the samples during the test.

EDX (Energy Dispersive X-Ray) mapping of Al/PA cross-section was performed on a TEM sample with STEM (Scanning Transmission Electron Microscopy) imaging at 200 kV accelerating voltage using a JEOL ARM200 CFEG equipped with a JEOL JED-2300 X-ray spectrometer.

3. Results and discussions

Fig. 4 shows the surface roughness measurements of Al and PA surfaces with different surface pre-treatments.

Considering Al in as-received condition, as rolling is the manufacturing process, so there is a significant difference in two measured directions, i.e., the roughness amplitude is not isotropic. However, for other surface treatments and more specifically for the laser-polished condition, the surface roughness amplitude does not depend on the scanning direction. As can be observed, by the implementation of the laser ablation process, the surface roughness is significantly increased while it is reduced by the laser polishing process. It should be noted that the roughness of PA samples is slightly increased by the laser treatment process while isotropy was maintained.

Fig. 5 depicts the top view of Al surfaces with different surface pre-treatments. The increase of surface roughness with the laser ablation process and flattening the surface asperities with the laser polishing process is visible.

Modification of surface chemistry is recorded in Fig. 6 for Al samples in the as-received and laser-polished conditions. A large increase in oxygen concentration and a decrease in carbon concentration show that laser polishing leads to both fine etching of carbonaceous contamination and oxidation of the surface. More precisely, the stoichiometry of the Al surface after treatment is very close to the one of alumina. This is confirmed by the high-resolution spectra of Al where the Al metal peak becomes hardly visible after laser polishing (not shown here). In the case of laser ablation of Al, an XPS analysis to compare the surface chemistry of Al surface before and after laser treatment was performed in a previous article. Whatever the ablation conditions, it showed a similar effect to the laser polishing treatment, i.e., a large increase in oxygen concentration and a large decrease in carbon concentration (Al-Sayyad et al., 2019).

XPS analysis of PA samples is presented in Fig. 7. There is no significant modification of the surface chemistry after the laser treatment process except for a slight oxidation effect. More precisely, a very slight increase in the oxygen concentration is observed, together with a slight decrease in the nitrogen concentration. High-resolution spectra of oxygen show that more C—O bonds are observed compared to C═O for laser-treated samples (not shown here). It is assumed that these new C—O bonds are coming from the degradation of pristine PA molecules after laser treatment. Therefore, laser treatment has a limited effect on the surface chemistry of PA; yet, a stronger effect on the PA structure in

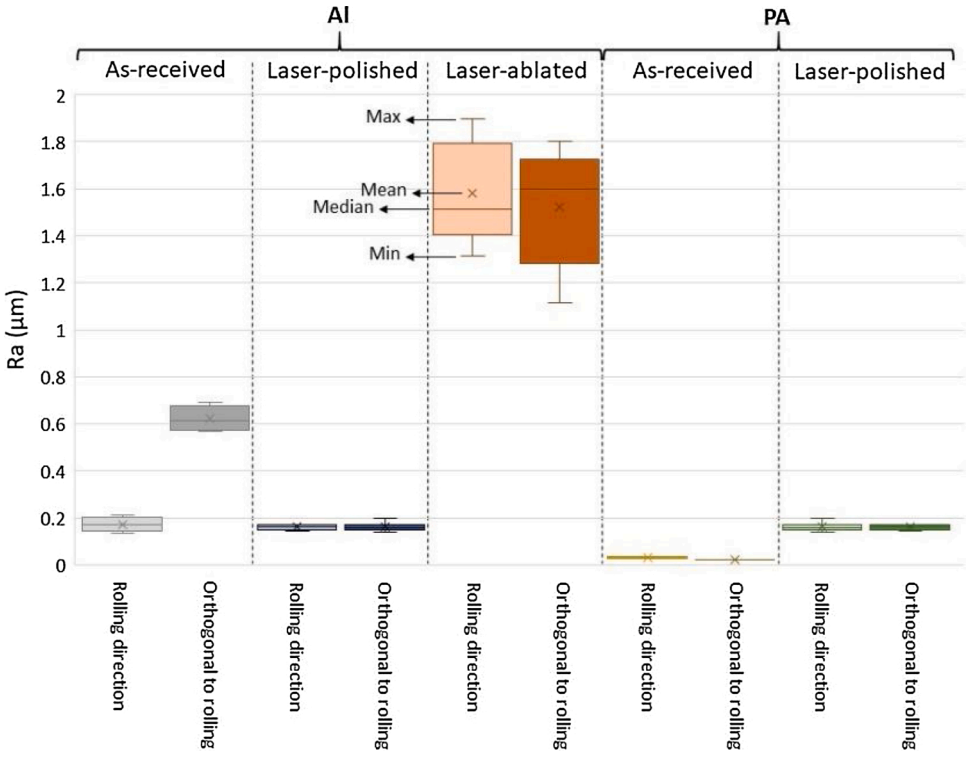

Fig. 4. Ra measurements of Al and PA for different surface treatments.

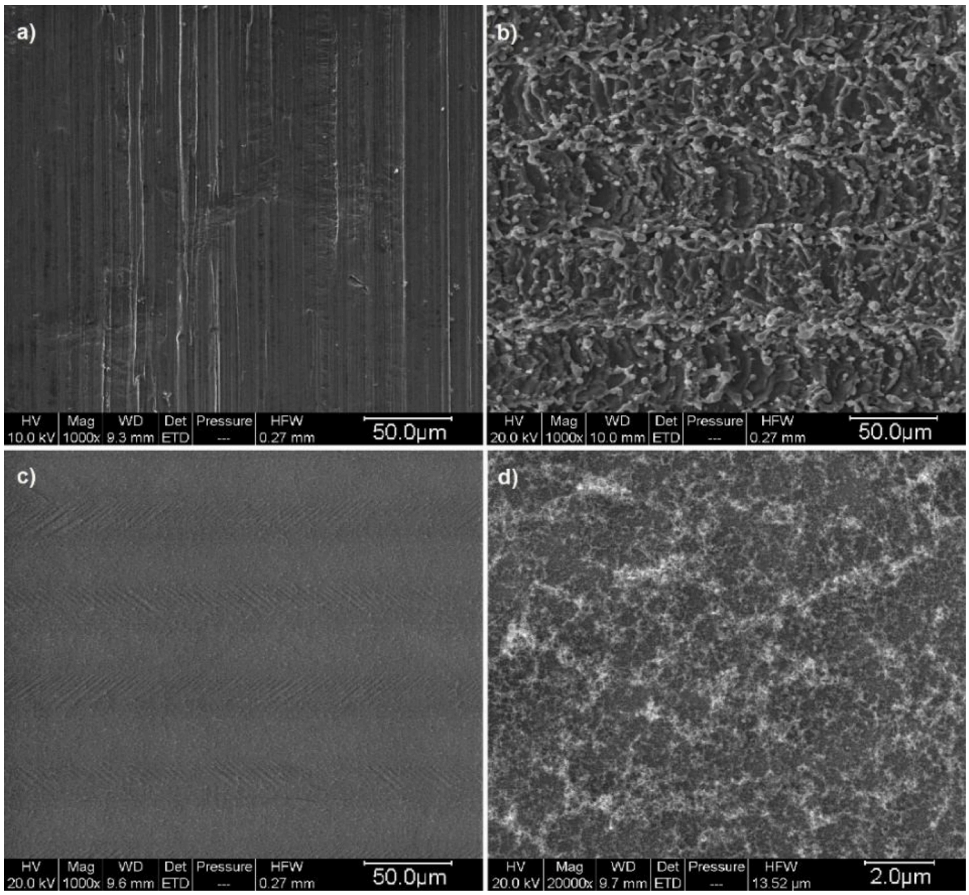

Fig. 5. Images of a) the as-received, b) the laser-ablated, c) the laser-polished, and d) the laser-polished surface with high magnification.

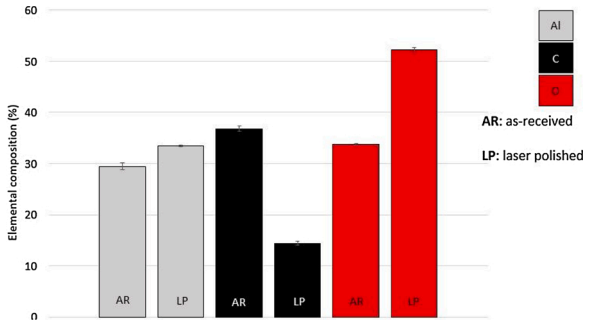

Fig. 6. Elemental composition of Al samples surfaces from XPS (error bars represent standard deviation).

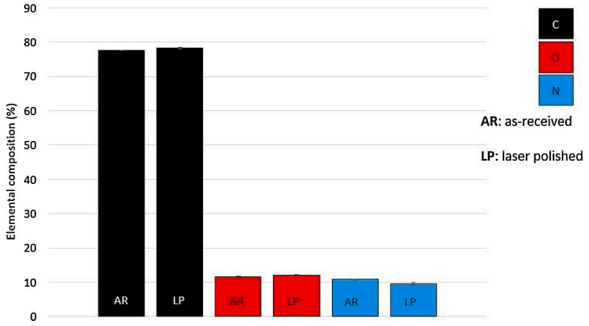

Fig. 7. Elemental composition of PA samples' surfaces from XPS (error bars represent standard deviation).

the first microns in depth is expected.

Fig. 8 shows the gXRD diffractograms of PA samples in grazing mode. PA is well-known as a semi-crystalline polymer. gXRD measurements conducted with a penetration depth of 35 μm before and after laser treatment on the PA surface show that the total crystallinity of PA slightly increases from 58.5 wt. % to 63.9 wt. %. The crystalline phase consists of the α phase (monoclinic) and the γ crystalline phase (monoclinic or pseudohexagonal). Although the total crystallinity has been increased by the laser treatment, the increase is associated with the γ phase (from 8.3 wt. % to 23.4 wt. %) and the ratio of α to γ phase reduced (from 85.8 wt. % to 63.4 wt. %).

Moreover, nano scratch indentations show the laser-treated area is softer than the as-received area (hardness of 175 MPa and 213 MPa, respectively). Both the slight increase of PA surface roughness and the decrease of hardness after the laser treatment process is certainly related to the evolution of the crystalline properties of PA to some extent. Indeed, as shown by gXRD, the laser treatment induced an increase in the γ phase fraction compared to the α phase. Since α phase is more stable and perfect (more packed) than γ phase (Lin and Argon, 1992), the laser treatment may locally slightly decrease the local packing of the crystalline phase explaining a local increase in roughness (local dilatation) and a local decrease of hardness (gamma phase expected to be less hard than alpha phase). This assumption is possible considering that this phase transition has more impact on roughness and hardness than the slight increase of the overall crystallinity (having the opposite influence). Other mechanisms are probably contributing to this increase of roughness and decrease of hardness.

Fig. 9 depicts the AFM imaging of the PA surface. For the as-received surface condition, no clear evidence of the crystalline structure is observed whereas a spherulitic structure is noted in the laser-treated area, as observed in Fig. 9a. For the latter image, in addition to apply a thermal treatment of the PA inducing crystalline changes in the volume of interaction, the laser can also finely etch the extreme surface of the polymer revealing its intrinsic morphology. In principle, to reveal semi-crystalline morphology, the amorphous phase has to be removed, creating a local topography since crystalline lamellae are still present. This mechanism may explain the increase of roughness, not only due to crystalline phase changes but also to this potential elimination of the amorphous phase at the extreme surface. Cryo-ultramicrotomy preparation is a convenient method to both get rid of the PA "skin", thereby removing the first tens of nanometers of the surface, and obtain a very flat surface which is convenient for AFM nanomechanical analysis.

An overview of both areas (laser-treated and as-received) after microtomy is observed in Fig. 9d. At low magnification, no evidence of the crystalline structure is visible in the untreated area, whereas the particular spherulitic structure is observed for the laser-treated area. Higher magnification is performed on the two areas, to investigate their nanostructure. A very fine structure, whose typical dimension is in the range of 50−100 nm, is observed for the untreated area (Fig. 9e and f), whereas another structure of greater dimensions (100−200 nm) is observed for the treated area (Fig. 9b and c). Both are assigned to the crystalline structure of the PA. Note that hardness measurement being a volume analysis, cannot depict this elimination of amorphous phase at the extreme surface.

As discussed by Amne Elahi et al. (2021), the as-received Al surface is covered by the natural oxide layer (25 nm thick) which is relatively dense and thin (Fig. 10a). Nevertheless, the laser polishing of the Al surface creates a smooth surface that is covered by the nano-structured artificial oxide layer. TEM images show that the artificial oxide layer (1.5 μm thick) is porous and much thicker than the natural one (Fig. 10b). It can be observed that there is no void or discontinuity between the laser-polished Al joined to PA, indicating that the porosity of the artificial oxide layer is effectively filled with the molten PA during

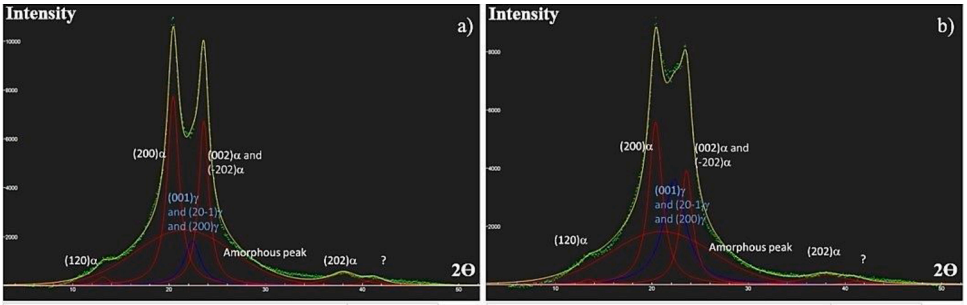

α phase crystallinity (wt. %)	50.2
γ phase crystallinity (wt. %)	8.3
Total crystallinity (wt. %)	58.5
α/γ ratio (%)	85.8

α phase crystallinity (wt. %)	40.5
γ phase crystallinity (wt. %)	23.4
Total crystallinity (wt. %)	63.9
α/γ ratio (%)	63.4

Fig. 8. XRD of the PA samples a) as-received condition, b) laser-treated condition.

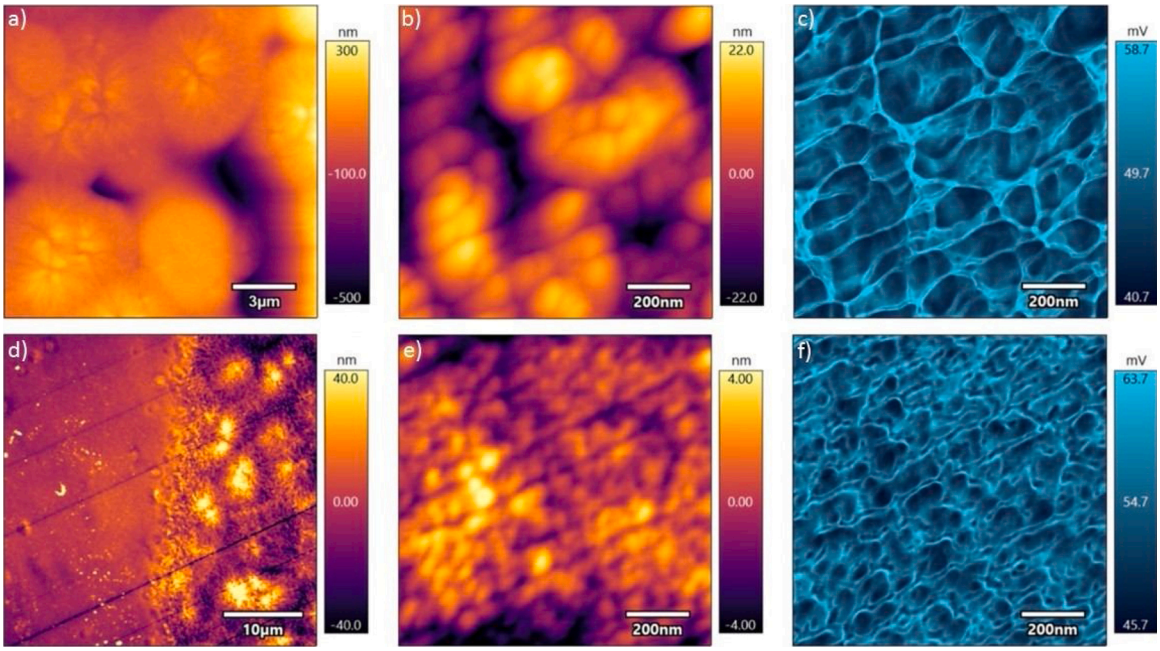

Fig. 9. AFM results of PA surfaces, a) laser-treated area on the bulk sample, no cryo-microtomy, topography, b) laser-treated area after cryo-microtomy, topography, c) laser-treated area after microtomy, dissipation, d) general view of both areas after microtomy: left untreated, right laser-treated, e) untreated area after microtomy, topography, and f) untreated area after microtomy, dissipation.

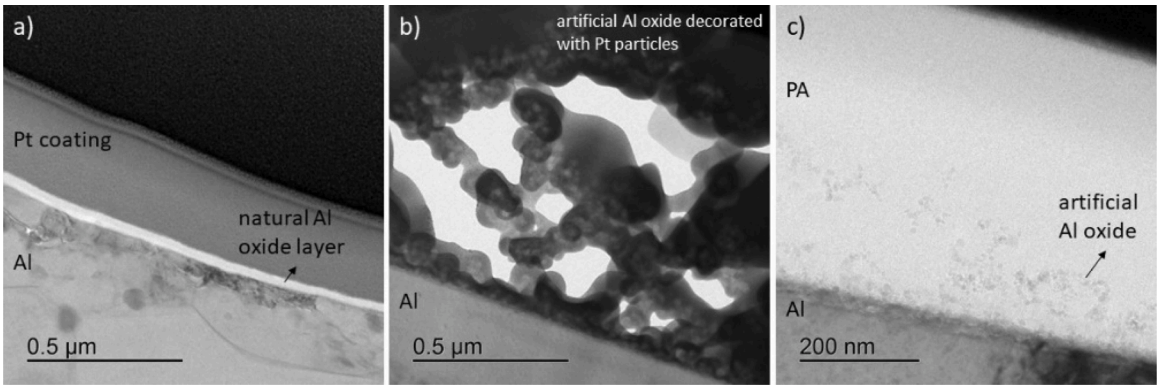

Fig. 10. TEM cross-section images of a) as-received Al, b) laser-polished Al, and c) laser-polished Al laser joined to as-received PA.

the joining process (Fig. 10c). Therefore, the artificial Al oxide layer provides an excellent infiltration site and a robust anchoring effect for PA.

Fig. 11 shows the shear load of different samples and Fig. 12 depicts the SEM imaging of Al fracture surfaces in a tilted view with the top view images of the selected areas. As can be inferred from Fig. 12, the adhesion of molten PA and Al surface is poor in as-received condition, resulting in a mixed adhesive/cohesive failure. It is due to the

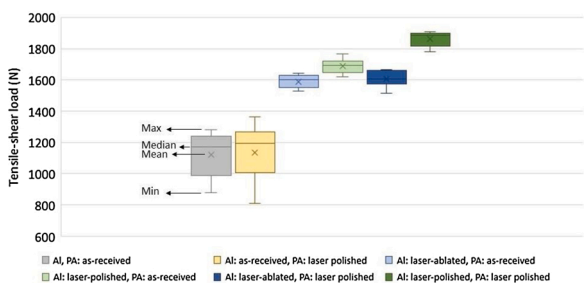

Fig. 11. Shear load of the samples.

characteristics of the natural Al oxide which is described earlier. By the implementation of either laser ablation or polishing on the Al side, the adhesion will be significantly improved thanks to the formation of an artificial Al oxide layer. Therefore, Al surface treatment is crucial to enhance the shear load of the joint which results in cohesive failure. It means that by applying the Al surface treatment (either by the laser polishing or the laser ablation processes), the joint between Al and PA is stronger than the PA near the joint area, and to increase the mechanical properties of the joined specimen, the PA structure should be modified near the joint area.

In other words, as the surface treatments of Al bring cohesive failure at PA, the adhesion of Al and PA at the interface can be considered similar for both Al surface treatments and the differences of the mechanical properties comes from the structure of PA at the failure zone. As discussed earlier, the PA surface treatment modifies the crystallinity close to the surface rather than the surface chemistry. Consequently, by merely modifying the PA surface structure without Al surface treatment, the shear load will not be noticeably improved due to unchanged wetting characteristics of PA to the as-received Al surface.

Fig. 13 shows the cross-section of different pre-treated Al samples

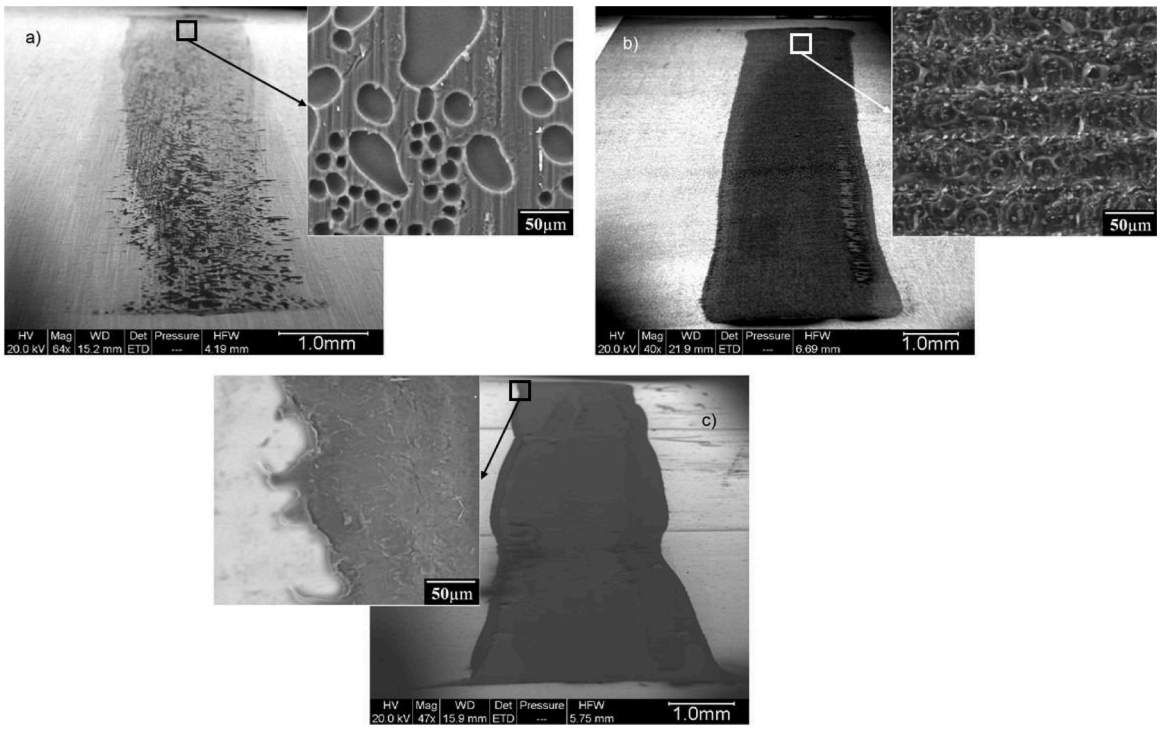

Fig. 12. Al fracture surfaces, a) as-received, b) laser-ablated, c) laser-polished condition in a tilted view with the top view of the selected areas.

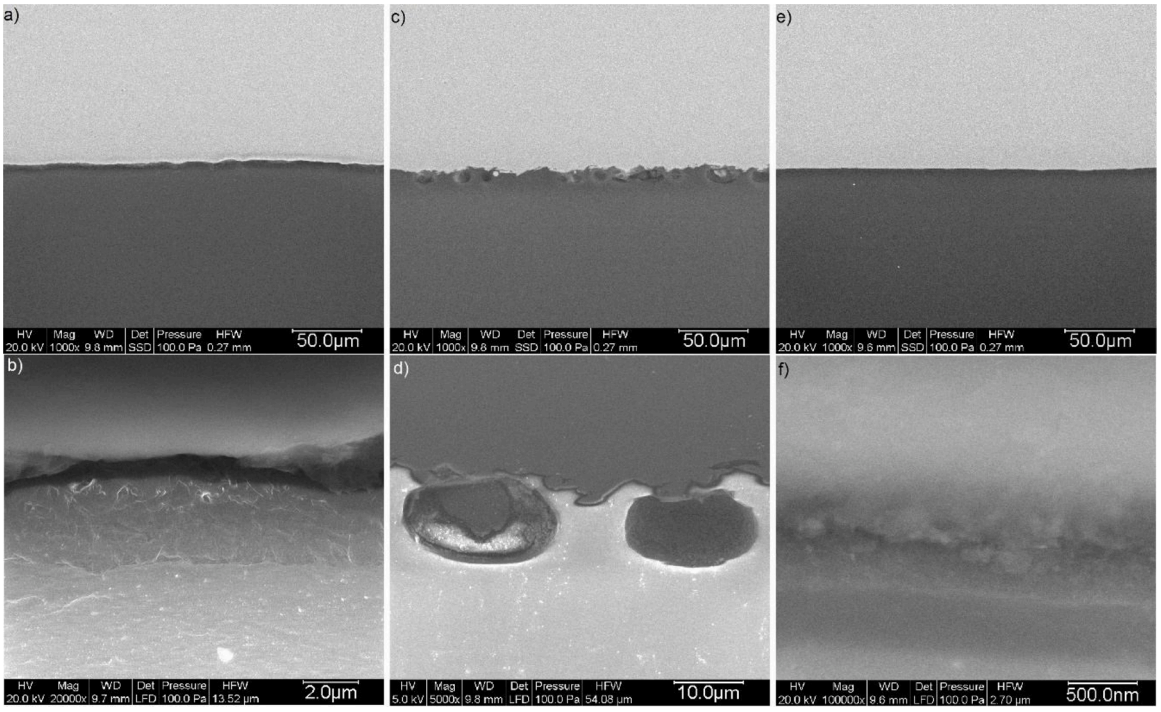

Fig. 13. Cross-section SEM images of Al-PA joined specimens, a,b)as-received Al, c,d) laser-ablated Al, e,f) laser-polished Al (in all figures Al is on top of PA).

joined to PA. All samples for this study were joined with the same joining parameters, however, in the case of laser-ablated Al joined to PA (Fig. 13c and d) some bubbles are visible near the interface of Al/PA. Considering their shape and location that is only in PA, these bubbles are generated due to local thermal degradation of PA based on uneven heat distribution from laser-ablated Al surface to PA which is promoted by high surface roughness.

To verify that the mentioned bubbles are found all along the join seam, µCT has been employed. Fig. 14 depicts the results of µCT analysis for different joined assemblies. Two pieces of information are provided: a representative 2D slice recorded in the interfacial region of Al/PA, and the 3D volume rendering of the bubbles extracted from the interfacial region after contrast thresholding. For the as-received Al, PA does not cover the Al at the interface of Al/PA uniformly as proved by the presence of discontinuities and bubbles (average equivalent diameter of 14.5 µm), which results in a mixed (adhesive/cohesive) failure. For laser-

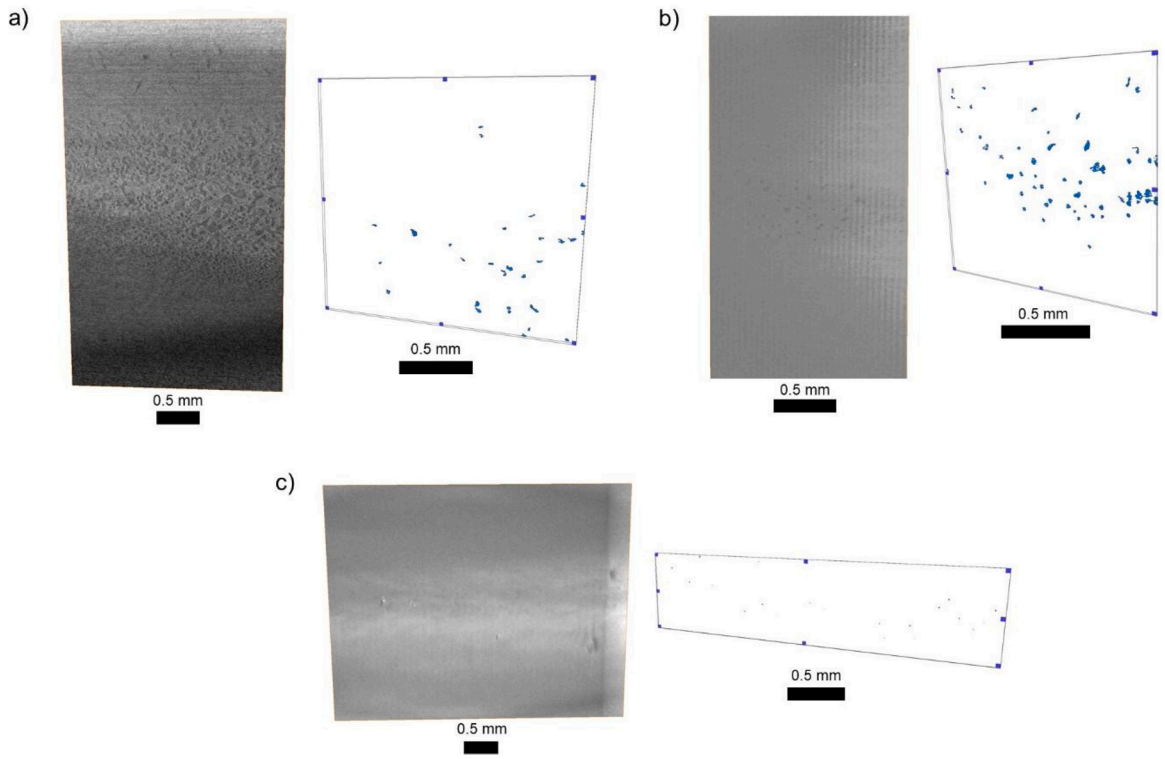

Fig. 14. μCT analysis at the interface of Al/PA showing for each case a representative interfacial slice (left) and the volume rendering of the interfacial bubbles (right) in the case of, a) as-received Al, b) laser-ablated Al, and c) laser-polished Al. (in all the samples, PA is as-received).

ablated Al, the presence of bubbles is confirmed (average equivalent diameter of 18.2 μm), while for laser-polished Al samples the interface is quite continuous and contains smaller bubbles (average equivalent diameter of 4.8 μm) compared to the two other cases.

Fig. 15 shows the fracture surfaces of the laser-ablated Al and as-received PA in the joined assembly after the shear test. The cross-sections of bubbles are visible on both surfaces. Therefore, although the failure during the tensile-shear test happens cohesively, the PA local degradation in the form of bubbles near the interface of Al/PA is responsible for the failure. The lower shear load of the laser-ablated samples compared to the laser-polished ones once joined to as-received PA, is due to different mechanisms of failure.

By combining the laser treatment of PA with the laser ablation of Al, there is no significant improvement of the shear load as shown in Fig. 11. It is assumed that the bubbles govern the joint failure in the case of Al ablation and the modification of the PA surface will therefore not significantly alter the failure mechanism.

For laser-polished samples joined to as-received PA, previous investigations show that the difference between the structures of the re-melted layer and the bulk PA is responsible for the failure, and it happens very few micrometers outside of the re-melted layer in the Heat-Affected Zone (HAZ) of PA. It is worth mentioning that by applying post heat treatment on the joined specimens, the shear load of the sample is improved (Amne Elahi et al., 2020). It is due to this fact that the re-melted layer for the current joining process is amorphous because of the high cooling rate (Amne Elahi et al., 2021). Fig. 16 depicts cross-sections images for the laser-polished Al samples joined to as-received and laser-treated PA. The depth of the laser-treated PA is approximately 50 μm while the thickness of the re-melted layer is approximately 30 μm.

Fig. 17 shows the force-displacement curves for the joined specimens with different surface treatments and the appearance of laser-polished Al joined to laser-treated PA. Compared to this sample, others represent relatively brittle failures. For as-received Al joined to as-received or

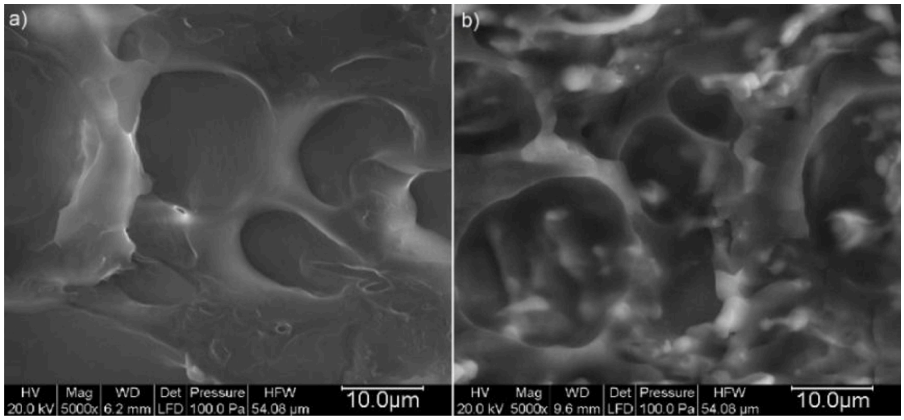

Fig. 15. Fracture surfaces of an Al/PA joined specimen with laser-ablated Al joined to as-received PA, a) PA surface, and b) Al surface after failure.

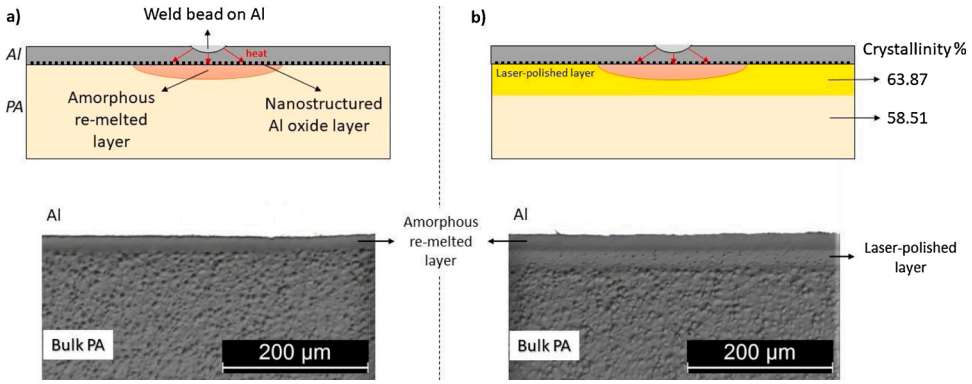

Fig. 16. Cross-section schematics and OM images, a) laser-polished Al joined to as-received PA, b) laser-polished Al joined to laser-treated PA.

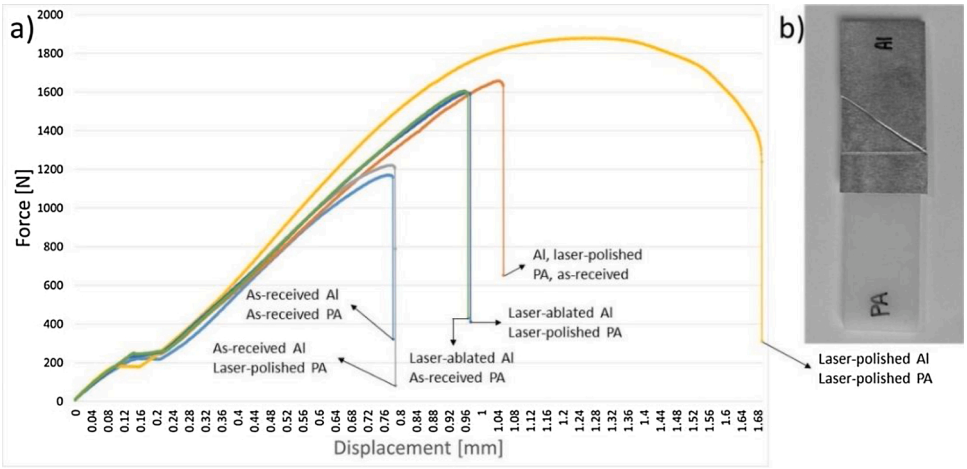

Fig. 17. Force-displacement graphs for different samples and b) the failure appearance of laser-polished Al joined to laser-treated PA.

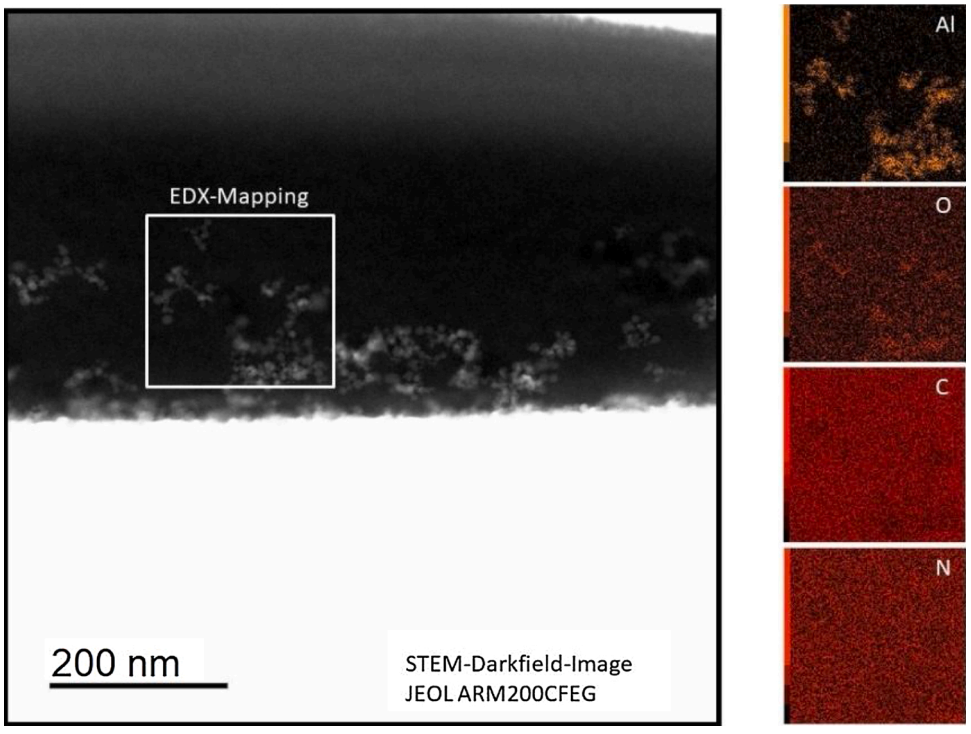

Fig. 18. STEM dark-field image of the Al/PA cross-section and elemental maps of Al, O, C, and N of the selected area.

laser-treated PA, poor and not uniform adhesion between the materials along the joining area is responsible for the failure. In the case of laser-ablated Al joined to as-received or laser-treated PA, the bubbles govern the failure and for laser-polished Al joined to as-received PA, the difference of crystalline structures between the re-melted layer and the bulk PA brings the failure at HAZ. As already discussed, laser treatment of PA leads to an increase in the crystallinity percentage of the PA surface. Therefore, HAZ is located in a more packed structure with higher mechanical properties in the case of laser-polished Al and laser-treated PA assembly, and it will improve the mechanical properties of the joints. Consequently, this modification of crystallinity probably prevents or delays the failure within PA and triggers the failure of Al in a ductile-shear manner.

To better understand the bonding of Al and PA after joining a cross-section (laser-polished Al joined to as-received PA) was prepared by FIB (Focused Ion Beam) and investigated by STEM dark-field imaging/EDX mapping (see Fig. 18). The nanostructured Al_xO_y on top of the Al substrate is completely wetted by PA, also indicated by the homogeneously distributed elements C and N surrounding Al and O visible in the elemental maps. Although there is no hint of a chemical change regarding the bondage of Al_xO_y to PA after joining, complete wetting of PA on top of the substrate indicates a strong physicochemical interaction between the nanostructured Al_xO_y and the PA. Together with the high surface area of nanostructured Al_xO_y, this leads to an exceptionally strong interconnection.

4. Conclusions

This study deals with the laser-based surface treatments of Al and PA before the laser joining of these two materials. The effect of these treatments on the failure mechanism is investigated when the Al-PA assembly is submitted to a tensile-shear test. It is concluded as followed:

- During the laser joining process, the adhesion is poor between the molten PA and as-received Al surface, thereby resulting in a mixed cohesive-adhesive failure of the joint. Adhesion is improved by applying the laser ablation or laser polishing on the Al surface, as evidenced by the cohesive failure of the joint. The surface analysis leads to the conclusion that enhanced adhesion is coming from the formation of an artificial oxide layer after Al laser treatments.
- The laser treatment of PA improves the degree of crystallinity (from 58.5 % to 63.9 %) in the first tens of microns in depth (the X-ray penetration depth was 35 μm while the re-solidified layer of PA due to laser treatment was measured to be 50 μm). The increase is associated with a great increase in γ phase concentration.
- Surface treatment on the Al surface individually enhances the shear load of the joint significantly, while laser treatment of PA coupled with as-received Al is not effective in this regard due to the low adhesion between molten PA and Al surface.
- Due to the high surface roughness of laser-ablated Al, the heat conduction from Al to PA is not uniform and results in local thermal degradation of PA in the form of distributed bubbles which are observed in PA near the interface of Al/PA. These bubbles are mainly responsible for the failure mechanism during the shear test of the joined assembly. Consequently, applying the laser treatment on the PA before joining assembled to laser-ablated Al, does not improve significantly the joint strength compared to untreated PA.
- The combination of Al laser polishing and PA laser treatment before the joining process results in the highest shear load of the specimens and the failure happens at Al base metal in a ductile manner. This leads to a remarkable increase of the joint strength, i.e., the increase of the load to failure is more than 60 % compared to the assembly of as-received materials. The laser treatment on the PA increases the crystallinity percentage of HAZ which is the susceptible area to fail and located between the re-melted layer and the bulk PA. Such reinforcement of the HAZ alters the mechanism of failure.
- Cross-section imaging/EDX analysis of the joint reveals a nano-structured Al_xO_y, that is homogeneously embedded in the PA matrix. This is explained by the complete wetting of PA on the laser-polished Al surface and results – together with the high surface area of the Al_xO_y nanostructures – in a very strong Al-PA interface.

CRediT authorship contribution statement

Mahdi Amne Elahi: Conceptualization, Methodology, Validation, Investigation, Data curation, Writing - original draft, Writing - review & editing, Visualization, Funding acquisition. **Marcus Koch:** Investigation, Data curation, Writing - review & editing, Visualization. **Julien Bardon:** Investigation, Data curation, Writing - original draft, Writing - review & editing. **Frédéric Addiego:** Investigation, Data curation, Writing - original draft, Writing - review & editing. **Peter Plapper:** Resources, Supervision, Project administration.

Declaration of Competing Interest

The authors report no declarations of interest.

Acknowledgments

The presented work is based on “Process Innovation for Sensors in Mobile Applications Based on Laser Assisted Metal-Plastic Joining’’ project (AFR-PPP grant, Reference 11633333). The authors like to thank Birgit Nothdurft (INM) for TEM lamella preparation and Jörg Schmauch (Universität des Saarlandes) for performing the STEM/EDX investigation. The authors from the University of Luxembourg would like to thank the support of the Luxembourg National Research Fund (FNR) and acknowledge Cebi Luxembourg S.A. as the industrial partner.

References

Al-Sayyad, A., Bardon, J., Hirchenhahn, P., Vaudémont, R., Houssiau, L., Plapper, P., 2019. Influence of aluminum laser ablation on interfacial thermal transfer and joint quality of laser welded aluminum-polyamide assemblies. Coatings 9, 768. https://doi.org/10.3390/coatings9110768.

Amne Elahi, M., Koch, M., Heck, M., Plapper, P., 2020. Pre and post-treatments to improve weldability and mechanical properties of Aluminum-Polyamide laser welded specimens. Procedia CIRP 94, 537–541. https://doi.org/10.1016/j.procir.2020.09.178.

Amne Elahi, M., Koch, M., Plapper, P., 2021. Evaluation of the joint based on different surface conditions for aluminum-polyamide laser welding. J. Laser Appl. 33 (012036), 1–8. https://doi.org/10.2351/7.0000326.

Arai, S., Kawahito, Y., Katayama, S., 2014. Effect of surface modification on laser direct joining of cyclic olefin polymer and stainless steel. Mater. Des. 59, 448–453. https://doi.org/10.1016/j.matdes.2014.03.018.

Bauernhuber, A., Markovits, T., 2012. Laser assisted joining of metal pins and thin plastic sheets. Phys. Procedia 39, 108–116. https://doi.org/10.1016/j.phpro.2012.10.020.

Bergmann, J.P., Stambke, M., 2012. Potential of laser-manufactured polymer-metal hybrid joints. Phys. Procedia 39, 84–91. https://doi.org/10.1016/j.phpro.2012.10.017.

Chen, Y.J., Yue, T.M., Guo, Z.N., 2016. A new laser joining technology for direct-bonding of metals and plastics. Mater. Des. 110, 775–781. https://doi.org/10.1016/j.matdes.2016.08.018.

Heckert, A., Singer, C., Zaeh, M.F., 2015. Pulsed laser surface pre-treatment of aluminium to join aluminium-thermoplastic hybrid parts. Lasers in Manufacturing Conference (LiM).

Heckert, A., Zaeh, M.F., 2014. Laser surface pre-treatment of aluminium for hybrid joints with glass fibre reinforced thermoplastics. Phys. Procedia 56, 1171–1181. https://doi.org/10.1016/j.phpro.2014.08.032.

Jung, K.W., Kawahito, Y., Takahashi, M., Katayama, S., 2013. Laser direct joining of carbon fiber reinforced plastic to zinc-coated steel. Mater. Des. 47, 179–188. https://doi.org/10.1016/j.matdes.2012.12.015.

Katayama, S., Kawahito, Y., 2008. Laser direct joining of metal and plastic. Scr. Mater. 59, 1247–1250. https://doi.org/10.1016/j.scriptamat.2008.08.026.

Kocun, M., Labuda, A., Meinhold, W., Revenko, I., Proksch, R., 2017. Fast, high resolution, and wide modulus range nanomechanical mapping with bimodal tapping mode. ACS Nano 11, 10097–10105. https://doi.org/10.1021/acsnano.7b04530.

Lambiase, F., Genna, S., 2017. Laser-assisted direct joining of AISI304 stainless steel with polycarbonate sheets: thermal analysis, mechanical characterization, and bonds morphology. Opt. Laser Technol. 88, 205–214. https://doi.org/10.1016/j.optlastec.2016.09.028.

Lin, L., Argon, A.S., 1992. Deformation resistance in oriented nylon 6. Macromolecules 25, 4011–4024. https://doi.org/10.1021/ma00041a025.

Penel Pierron, L., 1998. Deformation-Induced Phase Transitions in Hydrogen-Bonding Polymers: Ethylene Vinyl Alcohol Copolymers and Polyamide 6. PhD manuscript. Lille 1 university, France.

Rodríguez-Vidal, E., Sanz, C., Soriano, C., Leunda, J., Verhaeghe, G., 2016. Effect of metal micro-structuring on the mechanical behavior of polymer–metal laser T-joints. J. Mater. Process. Technol. 229, 668–677. https://doi.org/10.1016/j.jmatprotec.2015.10.026.

Roesner, A., Olowinsky, A., Gillner, A., 2013. Long term stability of laser joined plastic metal parts. Phys. Procedia 41, 169–171. https://doi.org/10.1016/j.phpro.2013.03.066.

Schricker, K., Bergmann, J.P., Hopfeld, M., Spieß, L., 2021. Effect of thermoplastic morphology on mechanical properties in laser-assisted joining of polyamide 6 with aluminum. Weld World 65, 699–711. https://doi.org/10.1007/s40194-020-01048-1.

Tan, X., Zhang, J., Shan, J., Yang, S., Ren, J., 2015. Characteristics and formation mechanism of porosities in CFRP during laser joining of CFRP and steel. Compos. Part B 70, 35–43. https://doi.org/10.1016/j.compositesb.2014.10.023.

Wang, H., Chen, Y., Guo, Z., Guan, Y., 2019. Porosity elimination in modified direct laser joining of Ti6Al4V and thermoplastics composites. Appl. Sci. 9 https://doi.org/10.3390/app9030411.

Yusof, F., Yukio, M., Yoshiharu, M., Hamdi, M., 2012. Effect of anodizing on pulsed Nd: YAG laser joining of polyethylene terephthalate (PET) and aluminium alloy (A5052). Mater. Des. 37, 410–415. https://doi.org/10.1016/j.matdes.2012.01.006.